Role of topology in complex functional networks of beta cells

Christian Cherubini,[1,2] Simonetta Filippi,[1,2] Alessio Gizzi,[1] and Alessandro Loppini[1]
[1]*Nonlinear Physics and Mathematical Modeling Laboratory, University Campus Bio-Medico of Rome, I-00128, Rome, Italy*
[2]*International Center for Relativistic Astrophysics Network—I.C.R.A.Net, University Campus Bio-Medico of Rome, I-00128, Rome, Italy*
(Received 4 February 2015; revised manuscript received 28 July 2015; published 5 October 2015)

The activity of pancreatic β cells can be described by biological networks of coupled nonlinear oscillators that, via electrochemical synchronization, release insulin in response to augmented glucose levels. In this work, we analyze the emergent behavior of regular and percolated β-cells clusters through a stochastic mathematical model where "functional" networks arise. We show that the emergence and robustness of the synchronized dynamics depend both on intrinsic and extrinsic parameters. In particular, cellular noise level, glucose concentration, network spatial architecture, and cell-to-cell coupling strength are the key factors for the generation of a rhythmic and robust activity. Their role in the functional network topology associated with β-cells clusters is analyzed and discussed.

DOI: 10.1103/PhysRevE.92.042702 PACS number(s): 87.18.Hf, 64.60.ah, 05.45.Xt, 64.60.aq

I. INTRODUCTION

The function of many biological systems underlies an intrinsic rhythmic activity [1–3]. These systems are not isolated but interact with the environment and other systems and show collective dynamics that emerges from a communicating network. Communication is the basis for the occurrence of synchronization or phase-locked dynamics of separate components in complex dynamical systems. Specifically, the role of structural and physical connections versus functional connectivity is currently investigated to understand and categorize the observed emerging behavior. In particular, the role of local heterogeneities [4], the spatial organization of the connectivity [5], and the inverse problem of extracting structural information from functional one [6] all aim at unveiling the key mechanisms responsible for synchronization and desynchronization in highly interconnected networks.

The β cells (BCs), in the endocrine islets of the pancreas, are an example of coupled nonlinear oscillators that show such a coordinated rhythmic activity. Pancreatic islets are ellipsoidal cells' aggregates characterized by a complex architecture. The islet contains at least three other types of cells other than BCs, i.e., α cells (ACs), δ cells (DCs), and pancreatic-polypeptide (PP) cells [7]. Several studies show that cells within the islet communicate both by autocrine and paracrine signaling, and by ultrastructural connections [7–9]. These communications finely control cells function, smooth cells heterogeneity, synchronize cells, etc. Specifically, BCs modify their electrical activity in response to changes in blood glycemic levels, triggering intracellular calcium oscillations and insulin secretion. The typical membrane voltage pattern observed in BCs is a "bursting" oscillation [7]. A key concept for this characteristic behavior is the interaction of fast and slow dynamics. The fast subsystem shows a bistability, i.e., the coexistence of two stable states, a periodic high-voltage solution, and a silent low-voltage steady state. Changes in the slow variable drive the fast subsystem between these two states, achieving a pattern of sustained high-voltage oscillations separated by quiescent phases. In this context, glucose acts like a control parameter that regulates the dynamics of the network itself. Glucose, in addition, exerts a crucial feedback on β-cell proliferation *in vitro* and *in vivo* [10].

In association with intrinsic biological noise and heterogeneity, the network topology strongly affects the single-node dynamics [5,11]. In fact, isolated BCs exhibit irregular spiking, but electrically coupled BCs in compact clusters show regular synchronous bursting leading to pulsatile insulin release [12,13]. In between these opposite behaviors, several emergent spatiotemporal patterns of electrical activity can arise from different network structures in terms of nodes number and connectivity. This aspect has a great relevance if one considers the dramatic topological effects that some pathological conditions can induce in BCs networks. Irregular behaviors caused by loss of coupling and degeneration of BCs is an example [14–16]. For instance, in type-1 diabetes, the loss of β-cell mass and communication leads to an insufficient insulin secretion and impaired pulsatility. This unstable phase can last from a few months up to several years [17], because β-cell populations larger than a critical size can still maintain the blood glycemic level in a physiological range [18,19]. Additionally, the islet architecture and composition, and hence the BCs networks, differ from species to species. In rodents, about 75% of islet cells are BCs and form a compact central core surrounded by ACs and DCs. In humans, BCs are about 54% of the islet cells and are organized in a sparse configuration [20–22]. These structural differences can play a key role in the generation of robust rhythmic behavior and the onset of local and/or global synchronous states. This thesis is corroborated by experimental evidences of (i) faster bursting [23] and (ii) spatially limited synchronization of intracellular calcium oscillations [21] in human BCs compared to rodents. Moreover, differences between mouse and human BCs in terms of ion currents also play a role in bursting oscillations.

In this work, bursting activity in BCs networks is studied via a stochastic mathematical model fine-tuned to reproduce mouse bursting activity [24]. The model is built through a percolation approach mimicking the physiological architecture of the islet. Emergent dynamics of BCs clusters are investigated by analyzing temporal correlations of cells' electrical activity and by deriving and constructing a functional network linking the BCs cluster structure to the emergent behavior. Through such an analysis, we provide a complete and quantitative description of the spatiotemporal synchronization properties

and their relation with experimental evidences. We show that very simple communication rules can give rise to complex functional coupling patterns within a stochastic framework and that the topology of these functional networks is very sensitive to changes in specific control parameters, i.e., the coupling conductance strength, the glucose concentration, and the noise strength. Such an approach, usually adopted to study the functional structure of the brain in physiological and pathological states [25–27], has been experimentally used to analyze the activity of BCs in islets from mouse pancreas tissue slices [28].

The paper is organized as follows. In Sec. II, the adopted stochastic mathematical model is presented. Glucose feedback and topological and functional networks architectures are described. In Sec. III, numerical simulations and results are presented. In Sec. IV, outcomes, limitations, and future perspectives are discussed. Conclusions are drawn in Sec. V.

II. MATHEMATICAL MODELING

In this section, we introduce a modified version of the minimal electrophysiological murine model SRK [24,29] that grasps many quantitative features of β-cells ensembles. The original model was designed to study isopotential cell populations and not fully synchronized cubic clusters in fixed normoglycemic conditions. As said before, the generalized version of the model here presented takes into account a fine-tuned glucose feedback and network structure based on cytoarchitecture evidences [20–22,30]. We finally explain how construct functional networks from the computed dynamics of these coupled oscillators.

A. SRK multicell model

SRK model equations are based on a Hodgkin-Huxley-type formulation [31], where a fast and a slow dynamics are nonlinearly coupled. Via this minimal modeling, it is possible to reproduce both the behaviors of isolated cells and the typical bursting electrical activity of cell clusters, thanks to the noise-filtering effect of BCs network. Each cell is described by three ordinary differential equations (ODE) and is coupled to other contiguous cells (see Appendix for details). The membrane potential and the potassium channels characterize the fast dynamics while the intracellular calcium concentration represents the slow variable that turns the cell in a silent or bursting regime. Several stochastic processes were implemented to model the gating of calcium-dependent potassium channels (K-Ca). This choice is originally due to the high conductance of this type of ion channels. Because of this, its stochastic gating leads to stronger perturbations of the membrane potential compared to K^+ and Ca^2+ channels. Following Portuesi *et al.* [11] and Loppini *et al.* [32], glucose feedback was modeled tuning the calcium removal rate parameter as a linear function of glycemic states. Heterogeneity is another important biological evidence. However, considering the intrinsic noise due to the stochastic gating of K-Ca channels, simulations performed on heterogeneous cells populations did not show significant differences from the activity observed in clusters of identical cells. Although, alternative approaches have been proposed in the literature [5], noise itself induces local heterogeneities [33] that overcome the effect of heterogeneity in cells parameters. For these reasons, in the following we consider homogeneous cells populations.

B. Numerical implementation

We have adopted the SRK model in order to simulate the BCs activity of different networks architectures. The numerical algorithm (see Appendix) for the integration of the network dynamics was implemented in C++ language. The Gephi software [34] and Matlab numerical environment were used for networks and data analysis, respectively. The *R* statistical tool was used for graphical purposes.

C. β-cell networks topology

The architectural organization of β cells in the islets differs from species to species [20]. BCs in murine islets are usually confined in a central core with a surrounding mantle of ACs and DCs. For the horse is exactly the opposite. Human islets instead are characterized by apparently random distributions of β, α, and δ cells, resulting in more complex islet structures [20]. In addition, also the islet composition is variable. As anticipated, the percentage of BCs in murine and human islets is about 75% and 54% [20–22], respectively. Another important architectural feature is that not all the adjacent BCs are coupled. In particular in mouse, about 33% of adjacent cells are not coupled [30]. Assuming a similar coupling distribution in human islets, we developed a β-cell insular geometry with a site-bond percolation [35] performed on a compact cubic cluster with a site occupancy probability of 54% ($p_s = 0.54$) and with a bond occupancy probability of 67% ($p_b = 0.67$). This procedure has been recently adopted in the context of pancreatic islet cellular networks [5]. In particular, phase transitions of BCs networks under different percolation conditions with the onset of type-1 diabetes have been related there. In this study, our aim is different. We fix the topological architecture of the network upon a given site-bond percolation and explore cells synchronization and emergent bursting, investigating the influence of architecture and parameters' changes on BCs functions.

The bond percolation effect has been experimentally studied in the literature [36,37], modeling the emergent dynamics with the use of deterministic BCs clusters. In particular it has been observed that: (1) in physiological conditions not all adjacent BCs are coupled; (2) inhibition or genetic knockout of gap junctions compromises synchronized cell activity; (3) cell aggregates size seems to be correlated with coordinated cells activity. We address this particular aspect with a complex network perspective, combined with stochastic dynamics and comparing and contrasting different representative architectures in terms of emergent behaviors for linear chains, compact clusters, and percolated structures.

D. Functional network analysis: A synchronization measure

Synchronization phenomena have been investigated computing the correlation index between all pairs of BCs

membrane potential signals [28,38]:

$$R_{ij} = \frac{\langle (V_i(t) - \langle V_i(t)\rangle)(V_j(t) - \langle V_j(t)\rangle)\rangle}{\sigma_i \sigma_j}, \qquad (1)$$

where σ_i is the standard deviation of $V_i(t)$. In the functional network approach, a new network, different from the structural physical cluster, is constructed on the basis of the correlation matrix obtained. Specifically, we add a link between separate cells if the temporal correlation of their electrical signals is greater than a threshold value. Following Stožer *et al.* [28], and filtering the stronger correlations, this value in our analysis is set to 0.8. From the functional network, one can achieve qualitative and quantitative information on the BCs emergent dynamics in terms of synchronized activity. In particular, the presence of synchronized subpopulations, the quantification of the temporal correlation of the global oscillatory activity, and several features of the emergent behavior can be derived.

For the sake of clarity, we list the observables specifically used in this study (see Refs. [39,40]): (i) the degree of the ith node $k_i = \sum_j a_{ij}$, where a_{ij} is the adjacency matrix associated to the network; (ii) the degree distribution $P(k)$ and the cumulative degree distribution $P_{\rm cum}(k) = \sum_{k'=k}^{\infty} P(k')$; (iii) the average nearest neighbors degree as a function of k, i.e., $k_{\rm nn}(k) = \frac{1}{N_k} \sum_{i,k_i=k} k_{{\rm nn},i}$, where $k_{{\rm nn},i} = \frac{1}{k_i} \sum_j a_{ij} k_j$, that is the average nearest-neighbors degree for the node i, and N_k is the node number of degree k; (iv) the average clustering coefficient $C = \frac{1}{N} \sum_i c_i = \frac{1}{N} \sum_i \frac{2e_i}{k_i(k_i-1)}$, where e_i are the edges in the subgraph of the neighbors of the ith node and $k_i(k_i-1)/2$ is the maximum number of edges in the subgraph.

As anticipated, the functional network topology is driven by cells synchronization, and we move from totally uncorrelated electrical activity to almost full synchronized behavior. Because of this, at least if the standard definition of the observables hold, we will also consider nodes of degree 0 (the isolated nodes) in the computation of the networks' statistics.

III. RESULTS

With the use of the site-bond percolation described above [35], a human-like insular structure was constructed from a compact cubic lattice of 1000 β cells. This procedure led to a fragmentation of the original architecture into separate components characterized by structural networks of different sizes and connectivities. The numerical study focuses on the analysis of the biggest component obtained, extracted from the percolated architecture, and formed by 260 cells (see Fig. 1). Two other simple topologies were constructed taking into account the same number of nodes: a linear 1D chain and a 3D compact cluster. In the latter case, a $7 \times 7 \times 7$ grid was sequentially filled with cells, stopping the cluster construction once the desired number of units was reached. A representation of the different topologies is shown in Fig. 2.

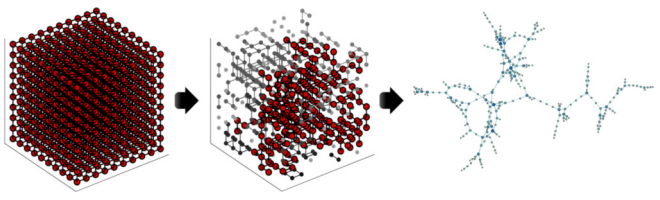

FIG. 1. (Color online) Construction of the percolated topology. Starting from a compact cubic cluster (left) a human-like architecture is obtained via a site-bond percolation (center) and the biggest connected component is extracted (right).

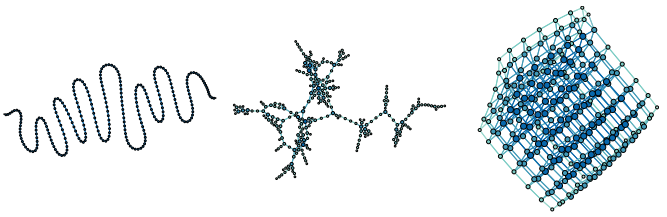

FIG. 2. (Color online) Different network topologies: linear chain (left), percolated architecture (center), compact structure (right).

In Fig. 3 the voltage time series computed for the stochastic SRK model is shown for a representative cell of any of the three simulated topologies. For these simulations a glucose concentration slightly above the BCs activation threshold was imposed ($[G] = 7.1$ mM, i.e., $k_{\rm Ca} = 0.03\ {\rm ms}^{-1}$), setting the coupling conductance between cells at a physiological value ($g_c = 215$ pS). Clearly, network topology strongly affects voltage oscillations. This effect is due to the different filtering properties induced by the "channel sharing" mechanism [24] with respect to the noise produced by stochastic channel gating. More organized structures give rise to longer bursting periods with lower variability of the interburst interval.

In order to extract information on the synchronization properties, in Fig. 4 we provide the correlation matrix, the computed functional network, and the space-time plots of voltage signals for each simulated structure. Bursting activity in the linear chain, Fig. 4(a), presents a short-range synchronization with excitation waves arising from different points in space and time, occasionally colliding. These evidences are supported by the structure of the functional network, which presents a mean node degree equal to 4 for the central cells of the chain. The opposite emergent behavior can be seen in the compact cluster, Fig. 4(c): the appearance of quasihorizontal bands in the voltage space-time plot highlights a long-range synchronization of the bursting. In this case, the

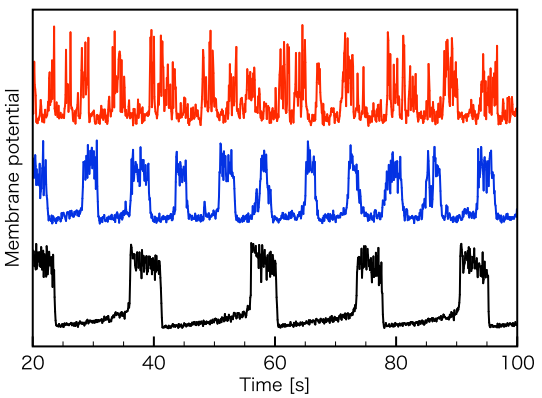

FIG. 3. (Color online) Membrane potential time series for a representative cell in: linear chain (top), percolated structure (middle), compact cluster (bottom).

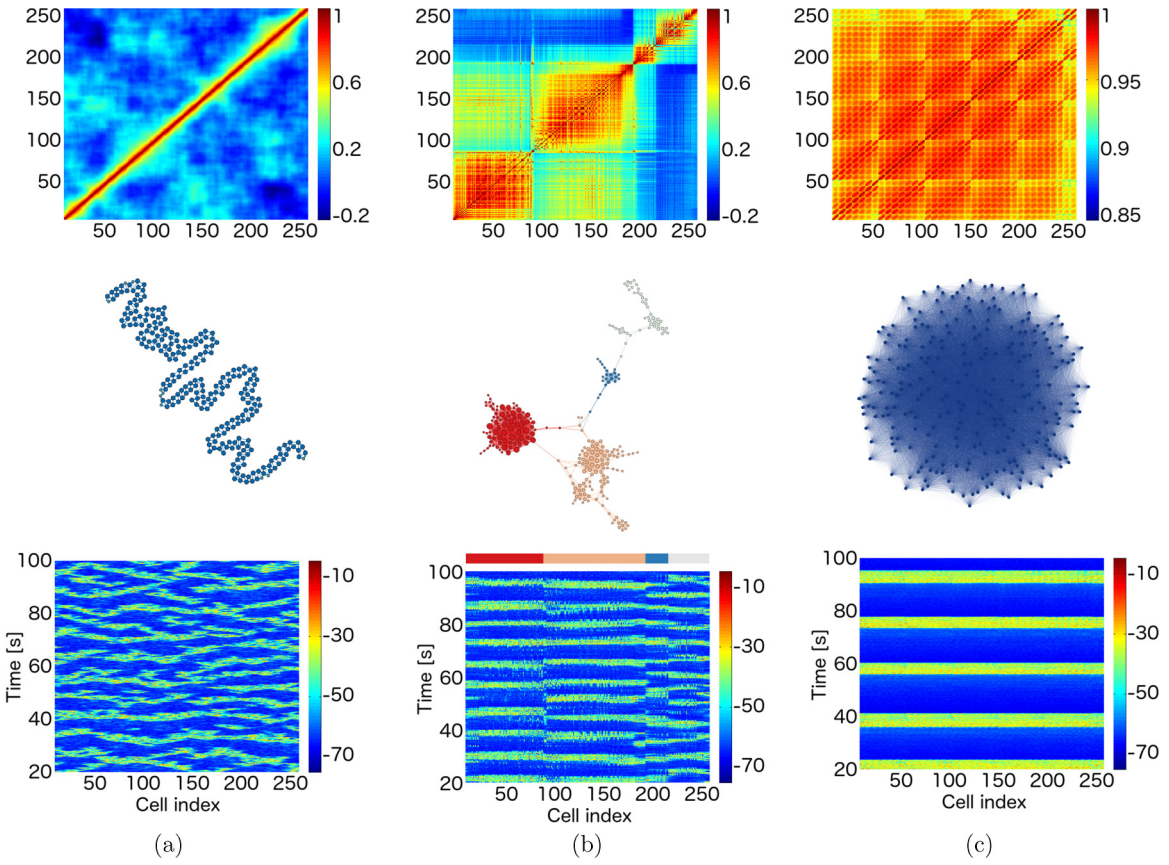

FIG. 4. (Color online) Correlation matrix (top row), reconstructed functional network (central row), and space-time plot of membrane voltage (bottom row) for each topology. (a) Left column: linear chain. (b) Central column: percolated topology. (c) Right column: compact structure. Physiological conditions are considered: $g_c = 215\,\mathrm{pS}$ and $[G] = 7.1\,\mathrm{mM}$. The color code of the percolated functional network identifies the subpopulations in the space-time plot.

x axis of the plot is a one-dimensional ordering of the cells obtained with a sequential indexing from the bottom to the top of the cluster. Functional network in such a situation is a fully connected network. The percolated topology shows instead an intermediate and very interesting behavior, Fig. 4(b). From the correlation matrix and the reconstructed functional network, four subpopulations with different bursting regimes can be identified (highlighted with different colors). The spatial coordinates of the space-time plot in this case were reordered on the basis of the macro subpopulations leading to the appearance of different out-of-phase bands of bursting activity. Each subpopulation is identified along the x axis by the same color used in the corresponding functional network.

A. Fixed glucose and variable gap junction conductance

Different functional networks were constructed analyzing the electrical activity of the BCs structures previously described, by varying the coupling strength (link strength of the structural network) and keeping fixed the glucose concentration ($[G] = 7.1\,\mathrm{mM}$). Figure 5 shows three functional networks sequences for the linear chain, the percolated network, and the compact cluster, respectively. The analysis shows that lowering g_c below a specific threshold causes the functional disconnection of the network. In this scenario, BCs do not show correlated activities nor robust bursting. Increasing the coupling conductance gives rise, instead, to functional connections that reveal a much more complex organization compared to the bare physical topology of the BCs cluster. Strongly interconnected functional communities appear from a limited number of junctional connections for the linear, the percolated, and the compact topology. The compact cluster gives rise to a fully connected functional network for all the coupling strengths considered, losing just a few connections at $g_c = 100\,\mathrm{pS}$, thus exhibiting a robust and synchronized bursting. The linear and the percolated cases, instead, do not reach a complete functional connectivity, even by increasing coupling strength. However, the study of the "functional" clustering coefficient computed for each operating condition highlights a similar trend in the network synchronization, as reported in Table I.

In order to further explore the emergent dynamics on the percolated topology, the degree distributions $P(k)$ of the functional networks are computed and shown in Fig. 6. Numerical results highlights that for a coupling conductance close to the physiological value ($g_c = 215\,\mathrm{pS}$), the distribution seems to match similar trends with respect to log-normal density functions and power-law decays. In order to better analyze this aspect, cumulative degree distributions were also computed for different coupling strengths. Log-Log plots of $P_{\mathrm{cum}}(k)$ are also reported together with a log-normal and a power law fit (straight line) of the data. Linear fitting seems

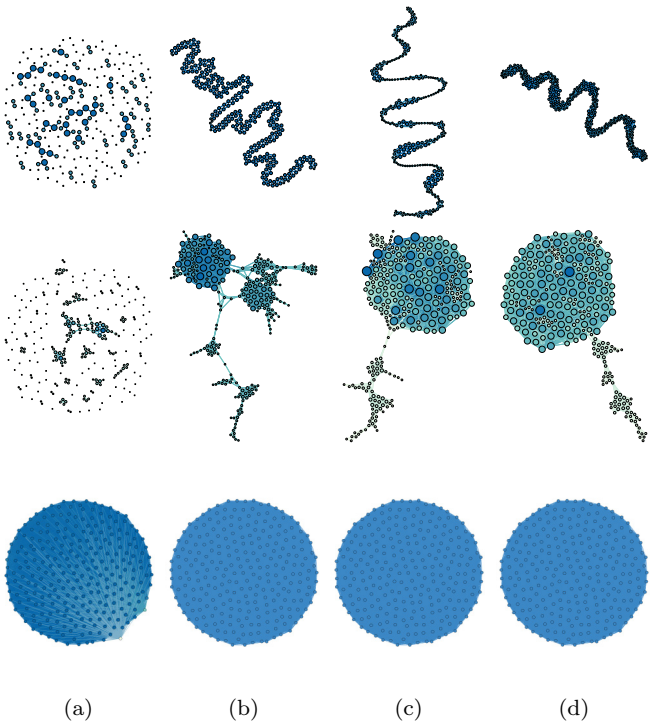

FIG. 5. (Color online) Functional networks sequences for increasing coupling strength, (a–d) $g_c = 100, 215, 300, 400$ pS, and fixed glucose concentration $[G] = 7.1$ mM. Top row, linear chain; center row, percolated structure; bottom row, compact cluster.

to hold for a central range of values while log-normal fit suits better for low degree nodes and the tail.

Although bigger cells populations should be studied to mitigate finite-size effects and to deeply investigate cumulative distributions behavior, our results highlight a strong inhomogeneity of the network and suggest that scale-free properties may be involved in the synchronization pathways. A bimodal distribution underlines bigger and more clustered synchronized communities, increasing the coupling strength further above the physiological value.

With the aim to study functional network correlations between degrees of connected nodes, the average nearest neighbor degree distributions $k_{nn}(k)$ are also computed and provided in Fig. 6. For a coupling strength in the range 100–215 pS, $k_{nn}(k)$ is an increasing function. For stronger coupling, the increasing trend reaches a plateau after a cutoff of $k \simeq 30$, probably linked to structural issues. However, this observation suggests an assortative mixing property of the network [39,41] for optimal coupling strength: nodes are mostly linked to other nodes with the same degree. Additionally, such assortative tendency is conserved in lower degree nodes for stronger coupling. Degree-preserving random rewiring (not shown) does not show increasing trend in $k_{nn}(k)$, suggesting that assortative mixing is not induced by the structure, but other processes may be involved [41].

TABLE I. Clustering coefficient for increasing coupling strengths ($[G] = 7.1$ mM). N600, simulations performed with 600 stochastic K-Ca channels per cell; N300, simulations performed with 300 stochastic K-Ca channels per cell.

	Linear		Percolated		Compact	
g_c [pS]	N600	N300	N600	N300	N600	N300
100	0.00	0.00	0.06	0.00	1.00	0.86
150	0.00	—	0.26	—	1.00	—
215	0.50	0.00	0.72	0.24	1.00	1.00
250	0.50	—	0.73	—	1.00	—
300	0.56	0.01	0.74	0.41	1.00	1.00
350	0.61	—	0.78	—	1.00	—
400	0.63	0.51	0.80	0.70	1.00	1.00

B. Fixed gap junction conductance and variable glucose

The emergent activity of the three structures was also analyzed for different values of glucose concentrations, ranging from low subthreshold stimulation values up to high glycemic levels that evoke a continuous spiking response. In this analysis, the coupling conductance was set at 215 pS. Figure 7 shows a functional networks sequence of the analyzed structures at different glycemic levels. Subthreshold values of glucose concentration functionally decouple the network as for low coupling strength values. In the same way, high values of glucose concentration decrease BCs temporal correlation causing functional decoupling of the network at high glycemic states. Optimal functional connectivity is obtained for glycemic levels slightly greater than the stimulation threshold. The computed clustering coefficient for each structure (see Table II) confirms these observations.

These results suggest that the glucose range ensuring cells functional synchronization is greater in the compact case, shrinking progressively in the percolated and the chain network. The analysis of the network degree distribution of the percolated cluster is computed for different glycemic states, see Fig. 8, showing that log-normal trends and possibly scale-free properties may also arise in the range of glucose values that maximize cells correlation. Cumulative distributions were not computed in this analysis because of the limited number of samples. In addition, although functional decoupling of the cells causes a lack of data for the computation of the average nearest-neighbor degree distribution in subthreshold stimulation and in overstimulation regimes, the computed $k_{nn}(k)$ shows an increasing trend for glucose concentrations just above the stimulation threshold. This result suggests an assortative property of the network as shown in the case of variable coupling strength discussed in the previous section.

C. Noise effect

Ion channel gating is a stochastic process, and the macroscopic currents observed originate from the opening and closing of large channel populations distributed on the cell membrane. Therefore, these biological systems can be viewed as intrinsically stochastic oscillators. Macroscopic membrane current fluctuations strongly depend on single-channel properties and on the numerosity of the population. Noise level is expected to have a great impact on cells synchronization.

On these bases, we investigate the noise effect on functional networks by varying the channel population size. Specifically,

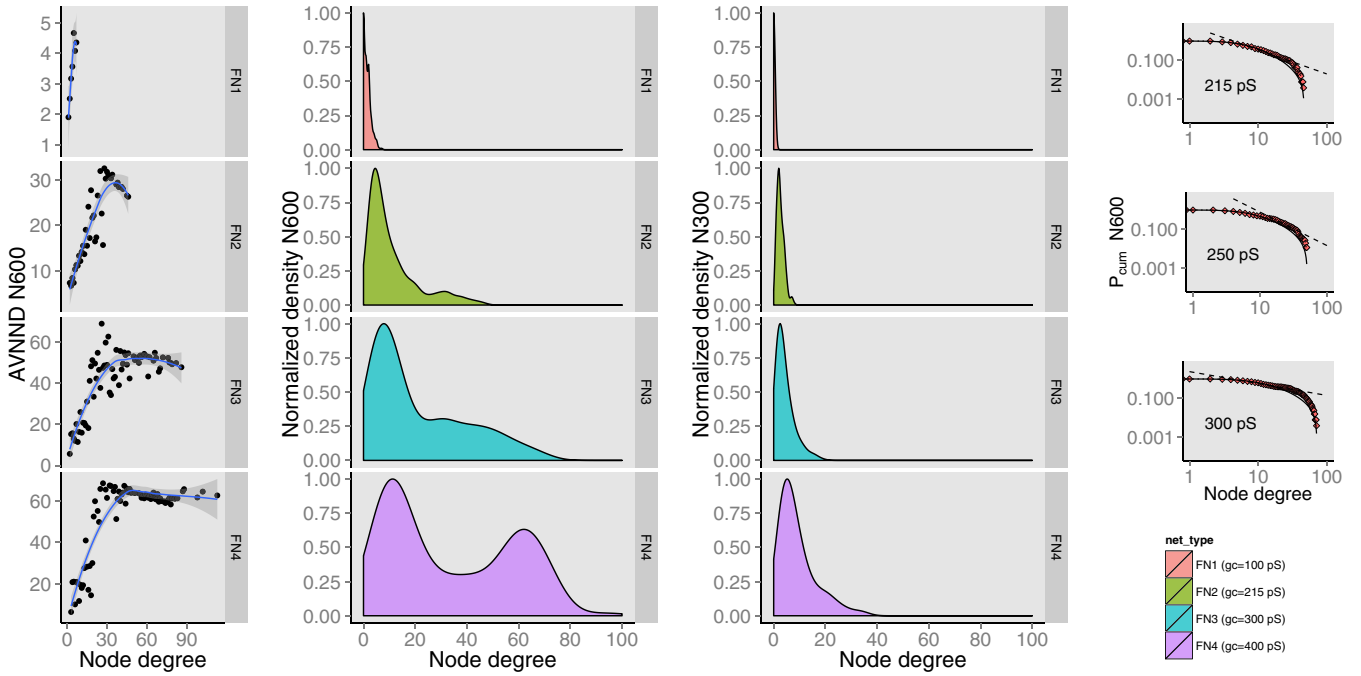

FIG. 6. (Color online) Degree distribution for different functional networks (FN) of the percolated structure varying the coupling strength ($g_c = 100, 215, 300, 400$ pS) and keeping fixed the glucose concentration ($[G] = 7.1$ mM). A smoothing kernel was used for the histograms fitting, previously normalizing the occurrences with the maximum value reached in each case. N600, observables computed from simulations performed with 600 stochastic K-Ca channels per cell; N300, observables computed from simulations performed with 300 stochastic K-Ca channels per cell; AVNND, average nearest neighbor degree; P_{cum}, cumulative degree distribution. Dotted line and continuous line in the AVNND plots represent a power law and a log-normal fit of the data (colored square), respectively.

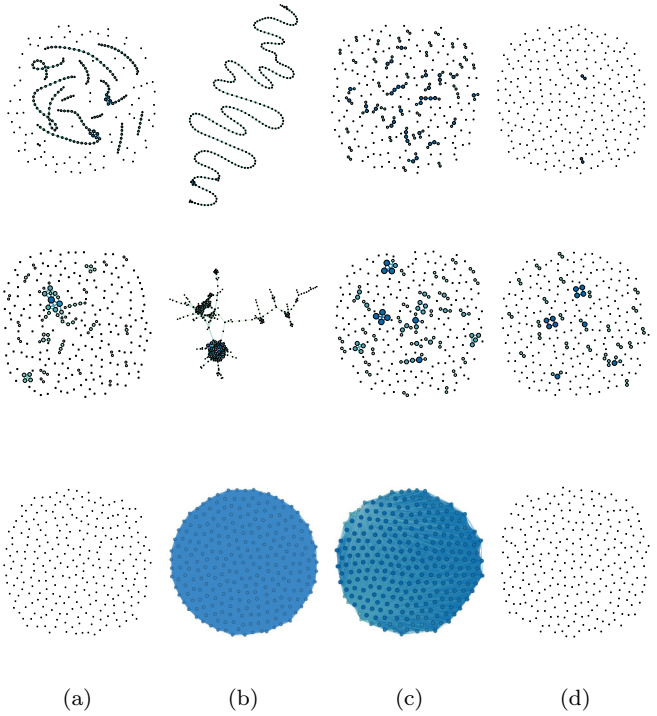

FIG. 7. (Color online) Functional networks sequences for increasing glucose concentration, (a–d) $[G] = 4.7, 8.7, 12.7, 16.6$ mM from left to right and fixed gap junction conductance $g_c = 215$ pS. Top row, linear chain; center row, percolated structure; bottom row, compact cluster.

the size of K-Ca channels population was lowered to half of the original value (from 600 to 300) in order to increase current fluctuations. Functional network sequences were similarly analyzed as presented above, i.e., (1) keeping fixed the glucose concentration and varying coupling strength, (2) keeping fixed the coupling strength and varying the glucose level. Numerical results show a similar trend with respect to lower noise levels. Figure 9 shows that increasing the coupling conductance enhances the connectivity of the network. Although, compared to the 600 K-Ca channels case, doubled values of the coupling strength are needed to achieve a similar functional connectivity for the linear and percolated structures. These observations are

TABLE II. Clustering coefficient for increasing glucose concentrations ($g_c = 215$ pS). N600, simulations performed with 600 stochastic K-Ca channels per cell; N300, simulations performed with 300 stochastic K-Ca channels per cell.

	Linear		Percolated		Compact	
Glucose [mM]	N600	N300	N600	N300	N600	N300
4.7	0.02	0.00	0.03	0.17	0.00	0.00
6.7	0.51	—	0.71	—	1.00	—
8.7	0.03	0.00	0.47	0.21	1.00	1.00
10.7	0.00	—	0.18	—	1.00	—
12.7	0.00	0.00	0.03	0.00	0.97	0.00
14.6	0.00	—	0.00	—	0.00	—
16.6	0.00	0.00	0.00	0.00	0.00	0.00

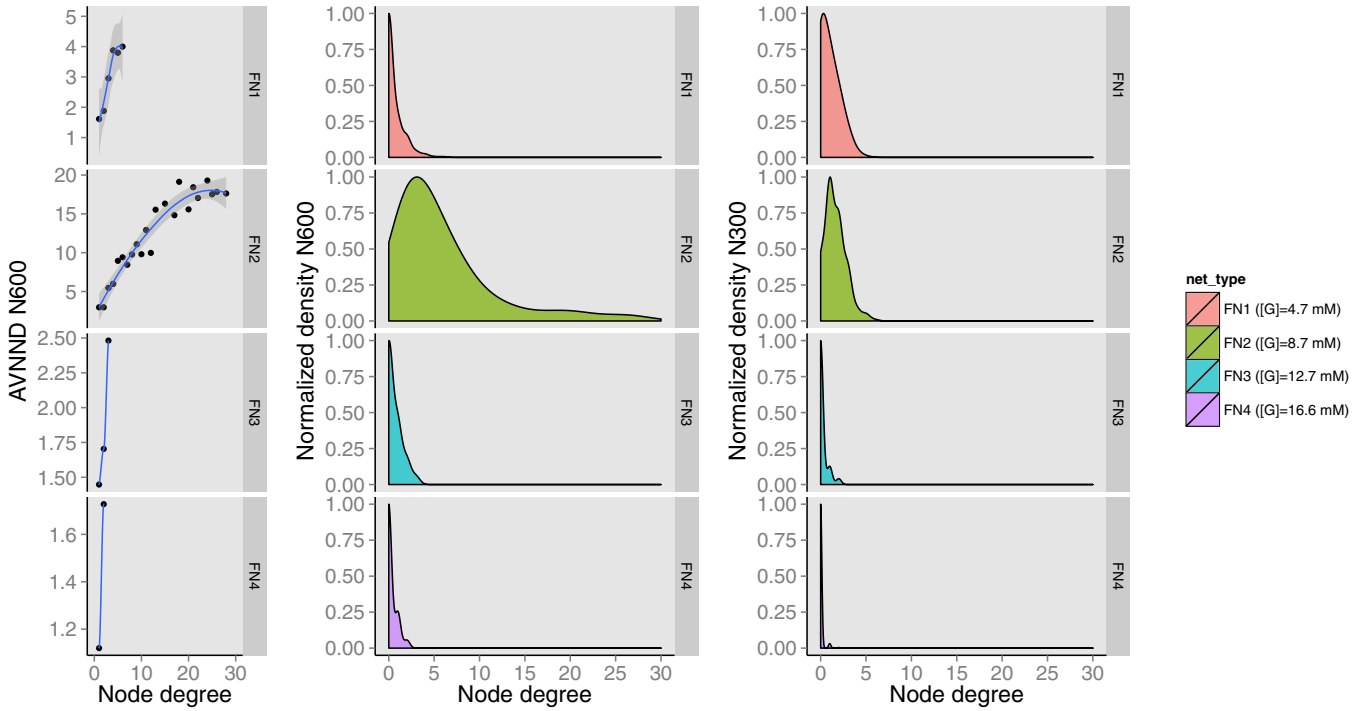

FIG. 8. (Color online) Degree distribution for different functional networks (FN) of the percolated structure varying the glucose concentration ($[G] = 4.7, 8.7, 12.7, 16.6$ mM) and keeping fixed the coupling conductance ($g_c = 215$ pS). As for variable coupling strength, a smoothing kernel was used for the normalized histograms fitting. N600, observables computed from simulations performed with 600 stochastic K-Ca channels per cell; N300, observables computed from simulations performed with 300 stochastic K-Ca channels per cell; AVNND, average nearest-neighbor degree.

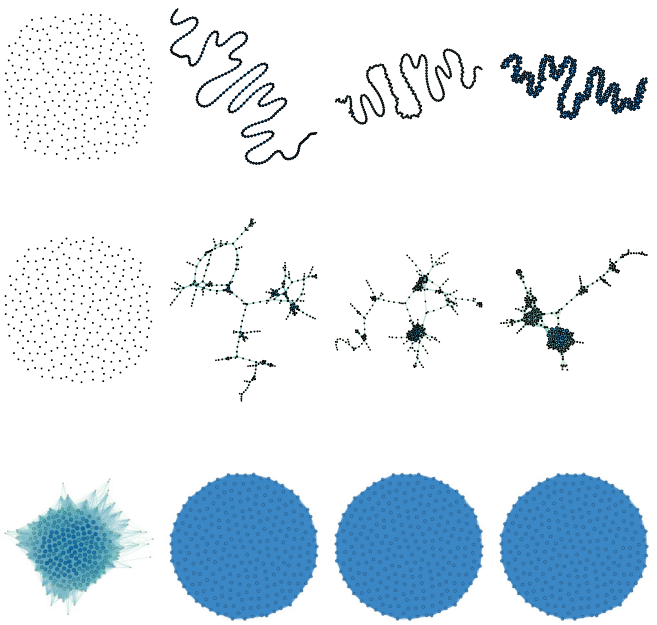

(a) (b) (c) (d)

FIG. 9. (Color online) Functional networks sequences for increasing coupling strength, (a–d) $g_c = 100, 215, 300, 400$ pS from left to right at fixed glucose, i.e., $[G] = 7.1$ mM. The number of K-Ca channels per cell was set to 300 to increase noise strength. Top row, linear chain; center row, percolated structure; bottom row, compact cluster.

summarized by the computed clustering coefficients reported in Table I. The compact cluster resulted more robust to noise perturbation, and a fully functional connectivity was reached for physiological values of the coupling conductance. The analysis was limited to selected values of the conductance due to computational issues.

Similar behaviors are also observed varying the glucose level (Fig. 10 and Table II). An optimal range of glucose concentration maximizing cells synchronization is still present. However, higher noise perturbations strongly reduce this range and the degree of synchronization.

The degree distribution analysis of the functional networks computed from the percolated structure (Figs. 6 and 8) shows similar topological properties also for enhanced noise levels. Log-normal and power-law behaviors of the degree distributions are obtained for coupling conductances higher than the physiological value and glucose concentrations of about 8–9 mM. However, also for higher noise levels the maximum degree of the nodes is significantly lowered. This result underlines the robustness of the functional topology with respect to perturbations.

IV. DISCUSSION

Experimental studies have shown that β cells in pancreatic islets exploit several pathways of communication in order to coordinate and synchronize their secretory activity, from electrical to autocrine and paracrine coupling. This evidence implies a specific structural organization of cells within the islet. Such a structure varies from species to species

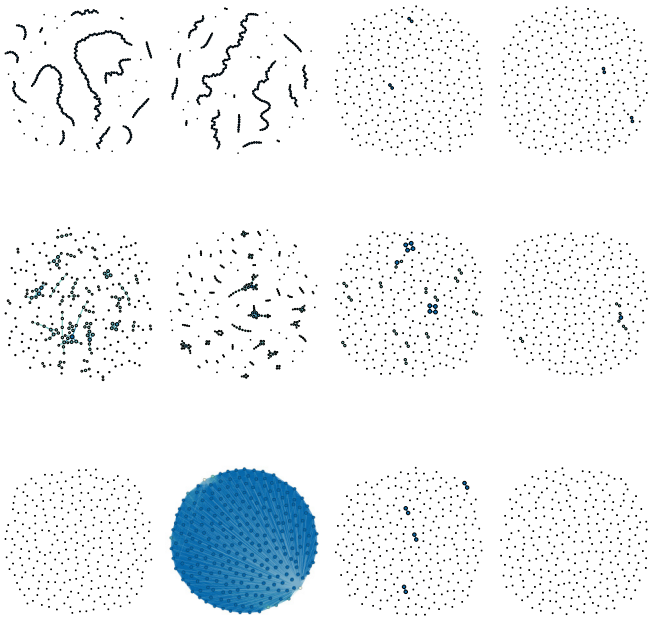

FIG. 10. (Color online) Functional networks sequences for increasing glucose, (a–d) $[G] = 4.7, 8.7, 12.7, 16.6$ mM from left to right at fixed gap junction conductance, i.e., $g_c = 215$ pS. The number of K-Ca channels per cell was set to 300 to increase noise strength. Top row, linear chain; center row, percolated structure; bottom row, compact cluster.

and can be substantially altered by degenerative pathologic processes like type-1 diabetes [42]. The existing literature on mouse and human data highlights that the emergent electrical activity in time and its coordination in space may vary significantly considering different species. Additionally, the loss of communication and degeneration of the cellular network in diabetic subjects strongly affect insulin release.

The present study analyzed the relation between structure and function in BCs networks, considering normal conditions and varying selected control parameters with respect to the physiological limits. In this framework, it is fundamental to analyze compact and percolated clusters since they clearly resemble mouse and human BCs architectures. The linear chain case, instead, is the representative example of a degenerate case, usually adopted to study the dynamics of coupled oscillators [43].

A. Bursting robustness

In the physiological state, numerical results show that temporal robustness of bursting activity is strongly affected by network architecture. This aspect was highlighted in the original work of Sherman *et al.* [24,29], studying cubic clusters of increasing size. They showed that coupled cells can "share the pool of stochastic channels" lowering noise strength. Similar behaviors were studied experimentally in cardiac coupled cells [44] and numerically in coupled networks of stochastic oscillators [24,29,45,46]. In these studies, an enhancement of the temporal precision was achieved for specific properties of the network, e.g., topology and number of nodes N. In particular, the standard deviation of the inter-beat intervals was shown to follow a $1/\sqrt{N}$ scaling law. Similar properties also arise in the stochastic gating of K-Ca channels in the "supercell" version of the SRK model [24]. Since the gating is modeled as a two-state process, it is possible to write the master equation for the evolution of the probability to find n channels in an open state in a population of size N [47]. The master equation is a set of $(N + 1)$ ODE of the form

$$\frac{dP_o(n,t)}{dt} = K_1 P_o(n-1,t) - K_2 P_o(n,t) + K_3 P_o(n+1,t),$$

where $K_1 = k^+(N - n + 1)$, $K_2 = k^+(N - n) + k^- n$, $K_3 = k^-(n + 1)$, and $k^{+/-}$ are the transition rates from the closed to the open state (see Appendix).

The equilibrium solution is given by the well-known binomial distribution:

$$P_o^{\infty}(n) = \binom{N}{n} p^n (1-p)^{N-n},$$

with $p = k^+/(k^+ + k^-)$. The coefficient of variation of this distribution is $\mathrm{CV} = \mathrm{SD}/m = \sqrt{(1-p)/(Np)}$, where SD and m are the standard deviation and the mean value, respectively. For the supercell model, the total number of stochastic channels is given by the number of channels per cell times the number of cells within the isopotential cluster. Using CV as a noise measure, for an increasing number of cells a lower spreading of P is obtained and the decrease of noise fluctuations is proportional to $1/\sqrt{N_{\mathrm{cell}}}$. A similar intuitive approach was also pointed out by Clay *et al.* [45]. These observations underline scaling laws similar to the one found in the variation of temporal precision, which are embedded in the intrinsic stochastic process of channel gating on the cell membrane. In this study, we show that the attitude of noise spreading and filtering, which gives rise to a robust bursting in time, is also dependent on the clustering of the network and not only on the population size. Our approach is in line with the heterogeneity studies recently discussed in Ref. [4].

B. Cluster synchronization

Synchronization analysis of bursting activity reveals interesting features. In particular, the linear chains do not ensure a long-range synchronization of cells and the functional network analysis suggests that a significant correlation in the activity ($R \geqslant 0.8$) holds just in a radius of about two cells. Alternatively, the compact structure shows that fully functional connectivity can be reached even considering only nearest-neighbors interactions. Of note is that such a feature is in line with recorded signals in mouse islets, showing an in-phase bursting over the whole islet [12,13]. Interestingly, the percolated topology (the closest to the human physiological one) presents intermediate behaviors where several synchronized areas arise. A globally synchronized activity is not achieved in this case as demonstrated by the degree distribution of the functional network (Fig. 6) and the out-of-phase bands in the space-time plot of membrane voltage signals (Fig. 4). These results suggest a limited and partially synchronized activity in human-like β-cell networks under

physiological conditions, in line with experimental recordings of intracellular calcium [21].

Could these results be a symptom of modularity? It is known that many biological networks show such a feature, which is strictly connected to the system robustness against system's perturbations [48], i.e., environment changes or altered dynamics of some nodes in the network. The functional network structure changes dynamically when the operating conditions change. The numerical analyses we conducted in this study demonstrate that if the cluster structure is not compact, values of the coupling conductance below a certain threshold are not able to synchronize cells anymore. In fact, the functional network for the linear and percolated cases are almost totally disconnected. On the other hand, higher values of the coupling are able to recover cells synchronization though the functional network loses its modularity. These evidences suggest the hypothesis of an optimal value of coupling strength, peaked at the physiological value, to maintain the functional features of the system.

In addition, other interesting properties arise keeping fixed the coupling strength while increasing glucose concentration. Glycemic levels that keep β cells in a silent state or evoke a continuous bursting lead to cells desynchronization in all the topologies analyzed; i.e., the corresponding functional networks are almost totally disconnected. For intermediate values of glucose concentration, however, the clustering coefficient for all three structures reaches a clear maximum. This last result suggests an optimal value, again, of the glucose-synchronization feedback. This level is above the stimulatory threshold and for the percolated and compact clusters is very close to the peak of glucose concentration usually observed after a meal [49,50]. These outcomes are consistent with experimental based functional network analyses in mouse islets [28], where time correlations of intracellular calcium variations between β cells are analyzed.

C. Percolated clusters and self-similarity

The associative behaviors pointed out for the average nearest-neighbor degree distributions highlight interesting aspects of synchronization pathways. The node-degree correlation suggests somehow that the emergent coordinated activity does not appear as a sharp transition in response to parameters changes but comes out as a nucleation-like process. For low values of the coupling strength, high-degree nodes are absent and low-degree nodes are coupled with other low-degree nodes, i.e., functional cell doublets and small coordinated pools. Increasing the coupling strength, the distribution of $k_{\mathrm{nn}}(k)$ shows a plateau and high-degree nodes appear. These nodes are equally linked to other nodes, suggesting that the system is reaching a global synchronization.

Degree distributions analysis performed for the different operating conditions reveal that physiological coupling strength values and postprandial glucose concentrations induce a scale-free-like topology of the functional network. Our representative human-like cluster, in fact, comes from a particular occurrence of the percolation process performed on a regular 3D lattice of cells [5]. Specifically, in order to match biological and histological evidences, a site percolation with $p_s^* = 0.54$ and a bond percolation with $p_b^* = 0.67$ was performed. Numerical studies about mixed site-bond percolation performed on different lattices showed that the pair (p_s^*, p_b^*) is very close to the percolation threshold curve in the p_s-p_b plane for the cubic lattice (Fig. 1 in Ref. [51]). Moreover, finite-size effects have been pointed out also in Ref. [5]. In typical percolation problems performed on infinite lattices, once this threshold is reached a big connected cluster spanning all the lattice emerges; the process can be viewed as a phase transition in physical systems [35]. Near this critical threshold, fractal shapes can arise characterized by self-similarity properties. Scale-free topology of the functional network may then be reminiscent of the underlying self-similar topological structure, and variations of the model parameters could enhance or disrupt such a property in this perspective. Experimental studies have highlighted the appearance of scale-free networks in many biological complex systems like metabolic reaction networks, gene regulatory networks, and functional connectivity in the brain [52–54]. In the latter case, the scale-free properties are associated with characteristic states of the neural activity.

In the pancreatic islets, such a functional structure highlights substantial differences between mouse and human. A modularity and scale-free topology of synchronization (we are talking about functional networks) could represent the best way to regulate cells' electrophysiological activity. In addition, the analyses performed with increased noise levels suggest that perturbations of the voltage dynamics can considerably desynchronize cells' activity due to stochastic fluctuations of ion currents. However, numerical simulations also highlight that the observed topological features of the functional networks are conserved both for the percolated and the compact structure. These evidences suggest that the system is robust, and synchronization patterns are qualitatively conserved when the intrinsic noise due to cell properties is enhanced. Though these results have been derived on simplified topological BCs networks and adopting a murine-based stochastic mathematical model, due to the similarity of the reaction-diffusion formulation, ionic currents and the order of magnitude of the coupling conductances [55] we expect, by analogy, our results may have relevance within a complete and more reliable human-based framework.

V. CONCLUSIONS

The functional network analysis performed on different cluster topologies of coupled BCs highlighted a deep connection between structure and function. Results on cell synchronization are in line with experimental studies performed on human and mouse islets, in which a partial and a complete synchronization was found, respectively. The degree of synchronization is not constant but varies together with operating conditions. The compact cluster acts as a unique functional unit that is very robust over a degeneration of coupling and desegregates only for subthreshold and very high values of glucose concentration. The percolated structure gives rise to limited synchronization of cells as observed in human. In this case, physiological values of coupling conductance and glucose concentration maximize cells synchronization also preserving modularity and scale-free properties of the functional connectivity.

In the present study, we adapted a well-known murine-based electrophysiological model to different cluster configurations in order to highlight the relation between structural and physical topology and functionality [6]. A fine-tuning of the model parameters matching different electrophysiological behavior is out of the scope of this work. Moreover, synchronization and emergent dynamics need further exploitation in future studies taking into account that the analysis of the functional connectivity, different from the physical one, requires a careful interpretation of the statistical analyses. However, it is important to remark that modularity and scale-free properties shown in this work arise only for physiological values of the parameters, thus implying a correct interpretation of the results. In addition, synchronization and emergent dynamics are fundamental for the correct functioning of β cells and their alteration is related to pathological conditions, i.e., diabetes.

Model limitations rely with the absence of the autocrine and paracrine communication pathways within the islet and the different endocrine cells. In this perspective, more realistic coupled network topologies of the islet should be reconstructed [56] or based on local dependencies [57,58], analyzing the functional response of the cells with human electrophysiological models [55,59,60] and analyzing networks properties from observed dynamics [61]. Accordingly, the model should be tuned on human data and different percolation structures should be studied in the context of evolutionary studies [62]. In addition, weighted networks without a correlation cutoff need also to be considered in forthcoming contributions in order to better characterize the in-phase and out-of-phase bursting behaviors, as well as partial synchronization phenomena.

ACKNOWLEDGMENTS

We acknowledge the support from the International Center for Relativistic Astrophysics Network (ICRANet) and Gruppo Nazionale per la Fisica Matematica (GNFM-INdAM).

APPENDIX

1. Electrophysiological SRK model

Here we list the SRK model's equations [24,29], expressed for a single cell. For the sake of notation, we denote variables V_i, n_i, Ca_i, simply as V, n, Ca; C_m the cell membrane capacitance; V the membrane potential; n is the potassium (K^+) channel gating variable; n_∞ the steady-state activation curve for the potassium channel; Ca the intracellular calcium (Ca^{2+}) concentration; $\bar{g}_K$, $\bar{g}_{\mathrm{Ca}}$, and $\bar{g}_{\text{K-Ca}}$ the whole cell ionic channels conductances for K^+, Ca^{2+}, and K-Ca, respectively; g_c the coupling conductance; V_{K} and V_{Ca} the potassium and calcium reversal potentials; λ a parameter used to fine tune the K^+ channels time constant; f is the fraction of free intracellular calcium; α is a conversion factor; k_{Ca} the calcium removal rate; K_d the ratio of the kinetic constants that regulate the K-Ca channels chemical process of opening and closing; V_{cell} and S_{cell} the volume and the surface of the cell, respectively, assuming a spherical geometry; F the Faraday constant and the factor 10 in the membrane capacitance expression is the capacitance per unit area ($f\,F\,\mu\mathrm{m}^{-2}$).

$$
\begin{aligned}
C_m \frac{dV}{dt} &= -I_{\mathrm{ion}} - \bar{g}_{\text{K-Ca}}\, p(V - V_{\mathrm{K}}) - g_c \sum_{j\in\Omega}(V - V_j)\\
\frac{dn}{dt} &= \lambda\left[\frac{n_\infty - n}{\tau_n}\right]\\
\frac{d\mathrm{Ca}}{dt} &= f[-\alpha I_{\mathrm{Ca}} - k_{\mathrm{Ca}}\mathrm{Ca}]\\
\langle p\rangle &= \frac{\mathrm{Ca}}{\mathrm{K}_d + \mathrm{Ca}}\\
I_{\mathrm{ion}} &= I_{\mathrm{K}} + I_{\mathrm{Ca}} = \bar{g}_{\mathrm{K}} n(V - V_{\mathrm{K}}) + \bar{g}_{\mathrm{Ca}} m_\infty h(V - V_{\mathrm{Ca}})\\
m_\infty &= \frac{1}{1 + \exp[(V_m - V)/S_m]}\\
h &= \frac{1}{1 + \exp[(V - V_h)/S_h]}\\
n_\infty &= \frac{1}{1 + \exp[(V_n - V)/S_n]}\\
\tau_n &= \frac{c}{\exp[(V - \bar{V})/a] + \exp[(V - \bar{V})/b]}\\
\alpha &= \frac{1}{2\,\mathrm{F}\,V_{\mathrm{cell}}}\\
C_m &= 10\,S_{\mathrm{cell}}.
\end{aligned}
$$

The adopted formulation considers three particular ionic channels: (i) the delayed rectifier K^+ channel (allows ions flux in a specific direction), (ii) the Ca^{2+} channel, and (iii) the K-Ca channel. The Ca^{2+} conductance is defined by the product of two sigmoidal functions: a steady-state activation curve m_∞, and a factor h, introduced to achieve a reasonable fit of experimental data. The K^+ conductance is regulated by the activation level n with time constant τ_n. The K-Ca conductance at a particular instant is given by the total K-Ca conductance $\bar{g}_{\text{K-Ca}}$ times the fraction of open channels p calculated by a parallel stochastic process described in the following section.

The last term in Eq. (2) takes into account the ultrastructural connections (gap junctions) between cells and tends to homogenize the voltage gradients between neighboring cells. The summation is evaluated in a neighborhood Ω of the cell and defined as a three-dimensional expansion of a two-dimensional Von Neumann neighborhood [63]. The numerical integration of the ODE system was carried out using a fourthorder Runge-Kutta solver and a fixed time step of 0.1 ms. A complete list of the model parameters can be found in Table III.

2. Coupled stochastic processes

The opening and closure events of each K-Ca channel were modeled as a Markov stochastic process [47]. For a single channel the following two-state kinetics was considered:

$$
C \underset{1/\tau_o}{\overset{1/\tau_c}{\rightleftharpoons}} O,
$$

where τ_o and τ_c are the mean time spent by the channel in an opened and a closed state, respectively. Considering a stochastic variable $s \in \{C, O\}$ in a time interval Δt, the

TABLE III. Model parameters.

Parameter	Unit	Value
Cell radius	μm	6.5
F	C mmol^{-1}	96.487
V_K	mV	−75
V_{Ca}	mV	110
$\bar{g}_K$	pS	2500
$\bar{g}_{\mathrm{Ca}}$	pS	1400
$\bar{g}_{K-\mathrm{Ca}}$	pS	30 000
g_c	pS	See text
V_n	mV	−15
s_n	mV	5.6
V_m	mV	4
s_m	mV	14
V_h	mV	−10
s_h	mV	10
a	mV	65
b	mV	20
c	ms	60
$\bar{V}$	mV	−75
λ		1.7
K_d	μM	100
f		0.001
τ_c	ms	1000
C_1	ms^{-1} mM^{-1}	6.3×10^{-3}
C_2	ms^{-1}	0.0147

probability that a channel in a closed state makes a transition in an opened state is given by

$$\frac{\Delta t}{\tau_c} = \mathrm{Prob}\{s = \mathcal{O}, t + \Delta t \mid s = \mathcal{C}, t\}.$$

Vice versa the probability that a channel in an opened state makes a transition to a closed one is given by

$$\frac{\Delta t}{\tau_o} = \mathrm{Prob}\{s = \mathcal{C}, t + \Delta t \mid s = \mathcal{O}, t\}.$$

A Monte Carlo simulation scheme [47] was adopted to evolve such a stochastic process. To ensure probability conservation, the resulting summation over the transition probabilities must be 1, so one can split the interval $[0,1]$ in regions related to a specific transition of the channel. A random number extracted uniformly in the interval $[0,1]$ can then be used to impose the change of the single channel state. A number of 600 K-Ca channels *per cell* was considered, and the state of every single channel at each integration time step was evaluated. As in Ref. [24], mean closing time was kept fixed and mean opening time was defined as a function of calcium concentration:

$$\tau_o = \tau_c \frac{\mathrm{Ca}_i}{\mathrm{K}_d}.$$

We remark that the calcium feedback is achieved directly weighing the transition probability of the channel. The number of opened channels at each time t was used to obtain the factor p in the membrane potential equation. A congruential generator characterized by a relatively high value of the period was adopted using the *ran2* routine given in Ref. [64] to ensure the randomness of the generated number sequence.

3. Glucose feedback

By varying the k_{Ca} parameter, a silent regime or an emergent bursting with increasing active phases can be obtained. Following Portuesi *et al.* [11], we fine tuned this property to model glycemic inputs. Setting $k_{\mathrm{Ca}} = 0.02\,\mathrm{ms}^{-1}$ and $k_{\mathrm{Ca}} = 0.09\,\mathrm{ms}^{-1}$ the model responds with a silent-active transition and an active-continuous spiking transition, respectively. These transitions in BCs occur at glucose concentrations of 5.5 mM and 16.6 mM, respectively. On these evidences, we assumed for simplicity a monotonic linear trend of k_{Ca} given by

$$k_{\mathrm{Ca}} = C_1[G] - C_2 \quad \text{for} \quad [G] \geqslant 2.33\,\mathrm{mM},$$

where

$$C_1 = 6.3 \times 10^{-3}\,\mathrm{ms}^{-1}\,\mathrm{mM}^{-1}, \quad C_2 = 0.0147\,\mathrm{ms}^{-1},$$

and $[G]$ is the glucose concentration.

[1] L. Glass, Nature **410**, 277 (2001).
[2] S. H. Strogatz and I. Stewart, Sci. Am. **269**, 102 (1993).
[3] S. H. Strogatz, SIAM J. Appl. Math. **50**, 1645 (1990).
[4] F. Scafuti, T. Aoki, and M. di Bernardo, Phys. Rev. E **91**, 062913 (2015).
[5] I. J. Stamper, E. Jackson, and X. Wang, Phys. Rev. E **89**, 012719 (2014).
[6] W. Lin, Y. Wang, H. Ying, Y. C. Lai, and X. Wang, Phys. Rev. E **92**, 012912 (2015).
[7] F. M. Ashcroft and P. Rorsman, Prog. Biophys. Mol. Bio. **54**, 87 (1989).
[8] L. Orci, R. H. Unger, and A. E. Renold, Cell. Mol. Life Sci. **29**, 1015 (1973).
[9] R. L. Michaels and J. D. Sheridan, Science **214**, 801 (1981).
[10] M. R. Metukuri, P. Zhang, M. K. Basantani, C. Chin, R. E. Stamateris, L. C. Alonso, K. K. Takane, R. Gramignoli, S. C. Strom, R. M. O'Doherty, A. F. Stewart, R. C. Vasavada, A. Garcia-Ocaña, and D. K. Scott, Diabetes **61**, 2004 (2012).
[11] R. Portuesi, C. Cherubini, A. Gizzi, R. Buzzetti, P. Pozzilli, and S. Filippi, Diabetes Metab. Res. Rev. **29**, 194 (2013).
[12] J. V. Rocheleau, G. M. Walker, W. S. Head, O. P. McGuinness, and D. W. Piston, Proc. Natl. Acad. Sci. U.S.A. **101**, 12899 (2004).
[13] P. Gilon, R. M. Shepherd, and J. C. Henquin, J. Biol. Chem. **268**, 22265 (1993).
[14] P. Meda, D. Bosco, M. Chanson, E. Giordano, L. Vallar, C. Wollheim, and L. Orci, J. Clin. Invest. **86**, 759 (1990).
[15] C. Vozzi, S. Ullrich, A. Charollais, J. Philippe, L. Orci, and P. Meda, J. Cell Biol. **131**, 1561 (1995).
[16] A. Nittala and X. Wang, Theor. Biol. Med. Model. **5**, 17 (2008).
[17] M. Knip, R. Veijola, S. M. Virtanen, H. Hyöty, O. Vaarala, and H. K. Åkerblom, Diabetes **54** (Suppl. 2), S125 (2005).
[18] A. Jansen, F. Homo-Delarche, H. Hooijkaas, P. J. Leenen, M. Dardenne, and H. A. Drexhage, Diabetes **43**, 667 (1994).
[19] F. C. Jonkers, J. C. Jonas, P. Gilon, and J. C. Henquin, J. Physiol. **520**, 839 (1999).

[20] D. J. Steiner, A. Kim, K. Miller, and M. Hara, Islets **2**, 135 (2010).

[21] O. Cabrera, D. M. Berman, N. S. Kenyon, C. Ricordi, Per-Olof Berggren, and A. Caicedo, Proc. Natl. Acad. Sci. U.S.A. **103**, 2334 (2006).

[22] M. Brissova, M. J. Fowler, W. E. Nicholson, A. Chu, B. Hirshberg, D. M. Harlan, and A. C. Powers, J. Histochem. Cytochem. **53**, 1087 (2005).

[23] L. C. Falke, K. D. Gillis, D. M. Pressel, and S. Misler, FEBS Lett. **251**, 167 (1989).

[24] A. Sherman, J. Rinzel, and J. Keizer, Biophys. J. **54**, 411 (1988).

[25] M. P. Van Den Heuvel, and H. E. Hulshoff Pol, Eur. Neuropsychopharm. **20**, 519 (2010).

[26] W. de Haan, Y. A. Pijnenburg, R. L. Strijers, Y. van der Made, W. M. van der Flier, P. Scheltens, and C. J. Stam, BMC Neuroscience **10**, 101 (2009).

[27] C. J. Stam, Neurosci. Lett. **355**, 25 (2004).

[28] A. Stožer, M. Gosak, J. Dolenšek, M. Perc, M. Marhl, M. S. Rupnik, and D. Korošak, PLoS Comput. Biol. **9**, e1002923 (2013).

[29] A. Sherman and J. Rinzel, Biophys. J. **59**, 547 (1991).

[30] M. Perez-Armendariz, C. Roy, D. C. Spray, and M. V. Bennett, Biophys. J. **59**, 76 (1991).

[31] A. L. Hodgkin and A. F. Huxley, J. Physiol. **117**, 500 (1952).

[32] A. Loppini, A. Capolupo, C. Cherubini, A. Gizzi, M. Bertolaso, S. Filippi, and G. Vitiello, Phys. Lett. A **378**, 3210 (2014).

[33] M. G. Pedersen, J. Theor. Biol. **235**, 1 (2005).

[34] M. Bastian, S. Heymann, and M. Jacomy, ICWSM **8**, 361 (2009).

[35] D. Stauffer and A. Aharony, *Introduction to Percolation Theory* (CRC Press, Boca Raton, FL, 1994).

[36] R. K. P. Benninger, M. Zhang, W. S. Head, L. S. Satin, and D. W. Piston, Biophys. J. **95**, 5048 (2008).

[37] T. H. Hraha, A. B. Bernard, L. M. Nguyen, K. S. Anseth, and R. K. P. Benninger, Biophys. J. **106**, 299 (2014).

[38] J. Lee Rodgers and W. A. Nicewander, Am. Stat. **42**, 59 (1988).

[39] A. Barrat, M. Barthélemy, and A. Vespignani, *Dynamical Processes on Complex Networks* (Cambridge University Press, Cambridge, 2008).

[40] S. Boccaletti, V. Latora, Y. Moreno, M. Chavez, and D. U. Hwang, Phys. Rep. **424**, 175 (2006).

[41] A. L. Barabási, *Network Science* (Cambridge University Press, Cambridge, UK, 2016), http://barabasi.com/networksciencebook/.

[42] G. C. Weir, D. R. Laybutt, H. Kaneto, S. Bonner-Weir, and A. Sharma, Diabetes **50**, S154 (2001).

[43] A. Pikovsky, M. Rosenblum, J. Kurths, and R. C. Hilborn, *Synchronization: A Universal Concept in Nonlinear Sciences* (Cambridge University Press, Cambridge, 2001).

[44] J. R. Clay and R. L. DeHaan, Biophys. J. **28**, 377 (1979).

[45] J. R. Clay and L. J. DeFelice, Biophys. J. **42**, 151 (1983).

[46] H. Kori, Y. Kawamura, and N. Masuda, J. Theor. Biol. **297**, 61 (2012).

[47] C. P. Fall, E. S. Marland, J. M. Wagner, and J. J. Tyson (eds.), *Computational Cell Biology* (Springer, Berlin, 2002).

[48] A. L. Barabási and Z. N. Oltvai, Nature Rev. Genet. **5**, 101 (2004).

[49] J. C. Brand-Miller, K. Stockmann, F. Atkinson, P. Petocz, and G. Denyer, Am. J. Clin. Nutr. **89**, 97 (2009).

[50] B. W. Wolf, P. M. Humphrey, C. W. Hadley, K. S. Maharry, K. A. Garleb, and J. L. Firkins, J. Nutr. **132**, 1219 (2002).

[51] Y. Y. Tarasevich and S. C. van der Marck, Int. J. Mod. Phys. C **10**, 1193 (1999).

[52] H. Jeong, B. Tombor, R. Albert, Z. N. Oltvai, and A. L. Barabási, Nature **407**, 651 (2000).

[53] N. Guelzim, S. Bottani, P. Bourgine, and F. Képès, Nature Genet. **31**, 60 (2002).

[54] V. M. Eguiluz, D. R. Chialvo, G. A. Cecchi, M. Baliki, and A. V. Apkarian, Phys. Rev. Lett. **94**, 018102 (2005).

[55] M. G. Pedersen, Biophys. J. **99**, 3200 (2010).

[56] A. Caicedo, Semin. Cell. Dev. Biol. **24**, 11 (2013).

[57] S. Shao, X. Huang, H. E. Stanley, and S. Havlin, New J. Phys. **17**, 023049 (2015).

[58] S. Havlin, H. E. Stanley, A. Bashan, J. Gao, and D. Y. Kenett, Chaos, Solitons Fractals **72**, 4 (2015).

[59] M. Riz, M. Braun, and M. G. Pedersen, PLoS Comput. Biol. **10**, e1003389 (2014).

[60] M. Riz, M. Braun, X. Wu, and M. G. Pedersen, Biochem. Biophys. Res. Comm. **459**, 284 (2015).

[61] M. Timme and J. Casadiego, J. Phys. A: Math. Theor. **47**, 343001 (2014).

[62] L. G. Alvarez Zuzek, H. E. Stanley, and L. A. Braunstein, Sci. Rep. **5**, 12151 (2015).

[63] J. Von Neumann, *Theory of Self-reproducing Automata* (University of Illinois Press, Champaign, 1966).

[64] W. H. Press, B. P. Flannery, S. A. Teukolsky, and W. T. Vetterling, *Numerical Recipes in C, The Art of Scientific Computing* (Cambridge University Press, Cambridge, 1992).